DOI: 10.1002/ ((please add manuscript number))
Article type: Research Article

# Regulating the Third Metal to Design and Engineer Multilayered NiFeM (M: Co, Mn, and Cu) Nanofoam Anode Catalysts for Anion-Exchange Membrane Water Electrolyzers

*Xiaoxuan Yang,*[Δ] *Jiashun Liang,*[Δ] *Qiurong Shi,*[Δ] *Michael J. Zachman,*[Δ] *Sadia Kabir, Junwu Liang, Jing Zhu, Benjamin Slenker, Max Pupucevski, Natalia Macauley, A. Jeremy Kropf, Hao Zeng, Derek Strasser, Deborah J. Myers,* Hui Xu,* Zhenhua Zeng,* Yushan Yan, and Gang Wu**

X. Yang, J. Liang, Q. Shi, B. Slenker, M. Pupucevski and G. Wu
Department of Chemical and Biological Engineering, University at Buffalo, The State University of New York, Buffalo, New York 14260, USA. E-mail: gangwu@buffalo.edu

M. J. Zachman
Center for Nanophase Materials Sciences, Oak Ridge National Laboratory, Oak Ridge, TN 37831, USA.

S. Kabir, M. Pupucevski, N. Macauley, D. Strasser and H. Xu
Giner Inc., Newton, Massachusetts 02466, USA. E-mail: hxu@ginerinc.com

J. Liang
Optoelectronic Information Research Center, School of Physics and Telecommunication Engineering, Yulin Normal University, Yulin, Guangxi 537000, China.

J. Zhu
Department of Materials Science and Engineering, National University of Singapore, Singapore.

A. J. Kropf and D. J. Myers
Chemical Sciences and Engineering Division, Argonne National Laboratory, Lemont, IL 60439, USA. E-mail: dmyers@anl.gov

H. Zeng
Department of Physics, University at Buffalo, The State University of New York, Buffalo, New York 14260, USA.

Z. Zeng
Davidson School of Chemical Engineering, Purdue University, West Lafayette, Indiana 47907, USA. E-mail: zeng46@purdue.edu

Y. Yan
Department of Chemical and Biomolecular Engineering, Center for Catalytic Science and Technology, University of Delaware, Newark, DE 19716, USA.

[Δ] These authors contributed equally.

**Abstract.** Alkaline anion-exchange membrane water electrolyzers (AEMWEs) for green hydrogen production have received intensive attention due to their feasibility of using earth-abundant platinum group metal (PGM)-free catalysts. Various PGM-free catalysts were explored for the challenging oxygen evolution reaction (OER); however, few can demonstrate satisfactory performance in real AEMWEs due to insufficient electrical conductivity and unfavorable interfaces with ionomers in three-dimensional porous electrodes. Herein, we incorporate the third metal into NiFe-based catalysts to regulate their electronic structures and morphologies, aiming to achieve sufficient OER activity and performance in AEMWEs. Unlike traditional NiFe-based catalysts, the ternary NiFeM (M: Cu, Co, or Mn) catalysts are featured with multiple layered structures and nanofoam network morphologies, consisting of highly OER-active amorphous Ni-rich oxide shells and electrically conductive metallic alloy cores. Density functional calculations further elucidate that the physical and electronic perturbations to the NiFe induced by a third element lead to a fine-tuning of the redox ability of the metal sites at the reaction centers, which breaks the scaling relationship between OH* and O* intermediates at the reaction centers. Thus, the unique structural configuration and electronic regulation simultaneously benefit catalytic activity and performance improvements. These NiFeM nanofoam catalysts demonstrated promising anode performance in actual AEMWEs, comparable to the $IrO_2$ reference, especially at high current densities. Notably, using various electrolytes (*e.g.*, KOH solution or pure water) for AEMWEs exhibited a different performance trend among studied NiFeM catalysts, likely due to dynamic changes of catalysts under various OER environments. This work provides a new concept for designing highly efficient OER PGM-free anodes *via* incorporating the third metal to current NiFe for tuning optimal electronic and geometric structures.

## 1. Introduction

Hydrogen production through water electrolysis is considered an eco-friendly, sustainable, and renewable energy technology.[1-3] However, the oxygen evolution reaction (OER) at the anode involves a four-electron transfer and is intrinsically sluggish kinetically, requiring a high overpotential to yield sufficient current density.[4-6] While Ir and $IrO_2$ have long been considered state-of-the-art OER electrocatalysts, their scarcity and prohibitively high cost hinder widespread application in water electrolysis.[7-9] Unlike proton exchange membrane water electrolyzers (PEMWEs), alkaline anion-exchange membrane water electrolyzers (AEMWEs) enable the use of low-cost and earth-abundant platinum group metal (PGM)-free catalysts for both the anode and cathode, representing a sustainable solution for clean hydrogen generation in the future. In particular, 3d-transition metals, especially Ni, Fe, Co, and Mn, have demonstrated promising OER activity and stability in alkaline media.[10-15] Although most current transition metal oxide catalysts exhibit promising OER activity in a concentrated aqueous alkaline solution in half-cells, their success can rarely be replicated in more practical membrane electrode assembly (MEA)-based AEMWEs.[16, 17] One of the reasons is that MEA tests in a practical electrolyzer are much harsher, with a higher voltage, over 2.0 V, often applied, which can cause severe corrosion of some supporting materials, such as carbon.

Furthermore, the currently insufficient MEA performance is also related to low electrical/ionic conductivities and poor interfaces with ionomers within 3D porous catalyst layers. In addition, porosities and morphologies favorable for efficient mass transfer and ionomer dispersion are critical for achieving high current density for practical hydrogen generation. Therefore, more effort is needed to further design and engineer highly efficient OER electrocatalysts for AEMWEs.

Establishing a relationship between the structure/composition of the OER electrocatalysts and their MEA performance is of primary importance for understanding the catalytic mechanisms and improving AEMWE performance.

Compared to traditional metal oxides, amorphous metallic alloys have been reported as promising OER electrocatalysts due to the abundance of unsaturated coordination sites at the surfaces, which are beneficial for the rapid binding of oxygen-containing intermediates, thus facilitating reaction kinetics.[12] Besides, amorphous metallic alloys are usually metastable due to their structural and chemical homogeneity, having excellent corrosion resistance in corrosive electrolytes.[18, 19] However, achieving high stability and adequate performance for long-term operation is still challenging due to the thermodynamic instability and poor conductivity of metallic glasses.[20] Modifying the amorphous metallic glasses with nanocrystalline domains or developing glassy alloys could effectively improve their performance. For example, a FeCo amorphous alloy for OER electrocatalysis in alkaline electrolytes increases reaction kinetics compared with its elemental Co counterpart.[21] The surface-enriched oxide species contribute more positively charged metal cations to bind intermediates during the OER process.[12, 22]

In addition to intrinsic catalytic activity, engineering catalyst morphology becomes critical for promoting overall OER anode performance by exposing more accessible active sites, providing favorable charge/mass transport, and establishing robust interfaces and electrode structures. Among others, self-supported three-dimensional (3D) nanowire networks, nanofoams, or metallic aerogels have been evidenced as promising electrocatalysts as their macropores provide numerous pathways for mass transfer, more accessible interior active sites, and more importantly, support-free anti-corrosion features.[7, 10, 23-25] Additional modification of the building block structure could significantly enhance the catalytic performance. For example, creating porous structures could further increase the number of available active sites; generating core-shell or alloy structures could induce a synergetic/electronic effect, and so on.[7, 25-28] The self-supported microstructure and flexibility in composition/microstructure modification of self-supported 3D materials are especially suitable for OER electrocatalysis and AEMWEs.

Here, we explored a concept to regulate the electronic structures and morphologies of conventional NiFe catalysts via incorporating the third metals such as Cu, Mn, and Co, aiming to improve their intrinsic activity, electrical conductivity, and mass transport within the OER anode in real AEMWEs. In particular, we developed a new class of multiple-layered ternary NiFeM (M: Co, Mn, or Cu) nanofoam OER anode catalysts, consisting of self-assembled ultrathin nanowire building blocks. Each nanowire contains multilayered core-shell structures consisting of amorphous oxide shells and metallic alloy cores, which can simultaneously improve OER activity at the surface and electrical conductivity through the core. The most intrinsically active NiFeCo catalyst contains a FeCo-rich alloy core covered by a Ni-rich CoNi metal intermediate layer and further by an amorphous FeCo-doped Ni oxide/oxyhydroxide layer. These unique, multilayered structures efficiently improve the OER electrocatalytic activity and stability. The outer layer of amorphous Ni oxides/oxyhydroxides provides numerous low-coordination sites to facilitate OER kinetics. The intermediate metallic NiCo layer and the FeCoNi core improve the electrical conductivity of the catalysts, accelerating the electron-donating process during the OER. Notably, the middle NiCo layer may lead to lattice distortions in the outmost oxide layer,[29] which could tune the adsorption/desorption energy of the oxygen-containing intermediates during the OER process.

Among various electrolyte environments employed to study catalysts, we found that the measured OER activities do not agree when using concentrated alkaline electrolytes in a half-cell and the MEA performance under diluted KOH and pure water in real AEMWEs. This observation suggests that the interfaces and microenvironments of catalysts with electrolytes are crucial for the *in-situ* constructed active species, showing different catalytic properties for the OER. In particular, when diluted KOH electrolytes were used for AEMWEs, all of the studied ternary NiFeM catalysts exhibited superior performance to the $IrO_2$ anode. The NiFeMn catalyst generated the highest activity, especially in the large current density range. In contrast, when using pure water as the AEMWE electrolyte, the NiFeCu catalysts exhibited comparable MEA performance to the $IrO_2$ anode at high current densities. The interesting observation requires more advanced *in-situ* and *Operando* spectroscopy studies in the future. Overall, the encouraging AEMWE performance achieved from these NiFeM anodes represents a critical step in developing low-cost AEMWEs for clean hydrogen generation.

## 2. Results and discussion

### 2.1. Catalyst synthesis, morphology, and nanostructure

The morphological evolution of NiFeM nanofoams is a spontaneous weaving process with increasing interconnectivity involving the progression from small core-shell nanoparticles to nanowires and eventually to porous networks (Figure 1a). In a typical synthesis, the ternary NiFeM nanofoams are synthesized *via* an environmentally friendly and scalable method using sodium borohydride ($NaBH_4$) as the reducing agent, metal salts as precursors, and water as solvents. $NaBH_4$ is a strong reducing agent that can simultaneously reduce all the metal precursor ions into metal compounds without adding other surfactants. A metallic alloy particle was first chemically reduced during the formation of multiple-layered architecture, forming the catalyst core. The residual metal precursors were then reduced to form a mixed-phase intermediate layer. In addition, due to the hydrolysis process in water, part of the outermost metals were converted to mixed oxides/hydroxides/oxyhydroxides. The dispersive core-shell nanoparticles are spontaneously self-assembled to prepare free-standing nanowires. A 3D network morphology was eventually constructed by stacking uniaxially aligned nanowires at different stacking angles. The synthesis method is time- and energy-efficient, as the products can be obtained in 5 min at room temperature using only water as the solvent. More importantly, this synthesis method can be easily scaled up, critical for industrial mass production.

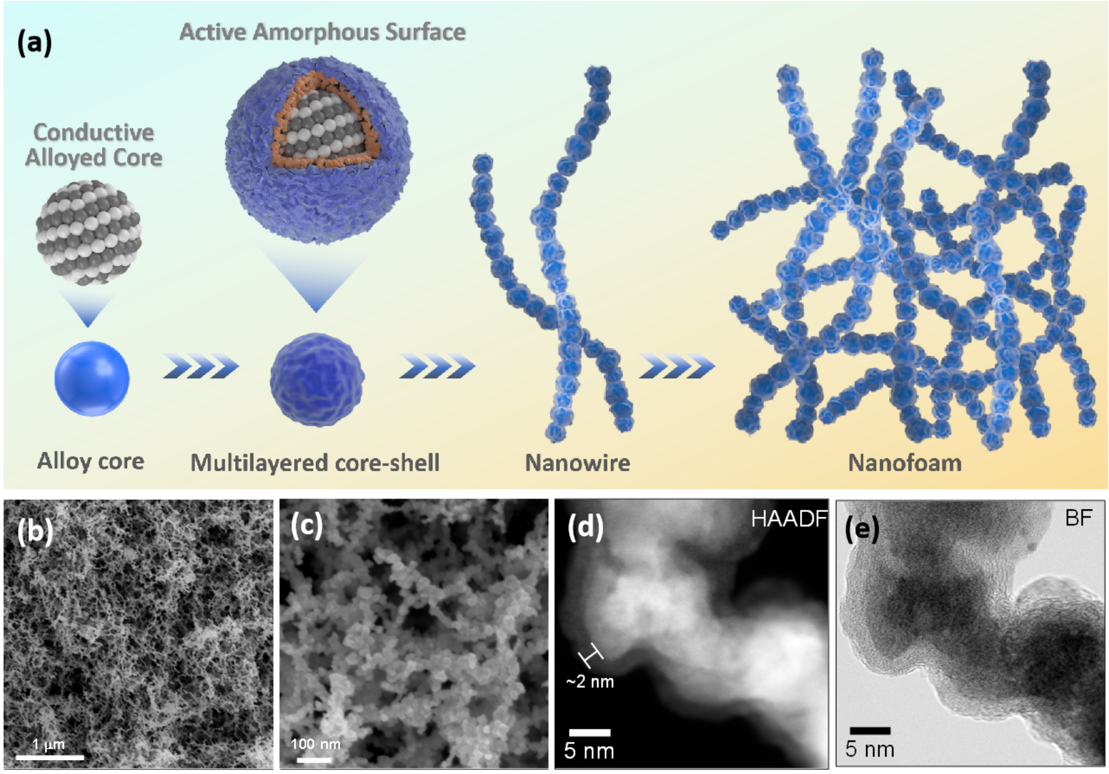

**Figure 1.** Ternary NiFeM metallic glass nanofoam OER catalysts with unique core-shell structures. (a) Schematic illustration of the formation of nanofoam-like NiFeM catalysts. (b-c) SEM images at different magnifications show porous network morphology. (d) HAADF-STEM and (e) BF-STEM images for a typical NiFeCo catalyst showing a well-defined ~2 nm thick amorphous oxide layer.

SEM images shown in Figures 1b-c indicate that the nanofoam-like NiFeM catalysts are composed of interconnected ultra-thin nanowires regardless of the third alloying metal – Co, Cu, or Mn (see also Figure S1). Unlike traditional transition metal oxide catalysts, the ternary NiFeM catalysts all display an abundance of meso- and macro-pores, with a surface area of around 30 $m^2g^{-1}$, as determined using the Brunauer-Emmett-Teller (BET) analysis (Figure S2). Mesopores of 2-50 nm and macro-pores of size >50 nm are desirable for mass transfer and could expose more interior active sites to improve overall mass activity. The detailed morphologies and nanostructures of NiFeM nanofoams were further analyzed by aberration-corrected scanning transmission electron microscopy (STEM). Figures 1d and 1e present representative high-angle annular dark-field (HAADF) and bright-field (BF) STEM images of the NiFeCo catalyst, respectively, showing that the interconnected nanowires are composed of core-shell structures with ~2 nm thick shells and ~20 nm thick cores.

STEM-based energy-dispersive X-ray spectroscopy (EDS) was employed further to analyze the unique, multilayered core-shell structures of these NiFeM catalysts. Figure 2 and Table S1 present a comprehensive STEM-EDS comparison of the nanostructure and distribution of chemical compositions within the NiFe and ternary NiFeM nanofoam catalysts. Introducing ternary metals changed the crystallinity and modified the catalysts into layered structures, with the elemental distribution in each layer depending on which ternary metal was added. For instance, the bi-metallic NiFe catalyst displayed an outside layer mainly composed of pure Ni oxide, followed by an intermediate Ni layer and a FeNi mixed-phase alloy core combining an amorphous structure (as evidenced by XRD pattern) with a few well-crystallized particles (as shown in Figure 2a and Figure S3). In contrast, ternary NiFeM catalysts often showed more complicated layered structures. The NiFeCu nanowires, for example, displayed a four-layered structure (Figure 2b). Ni oxide is located in the outermost layer as a well-defined shell with a thickness of ~2 nm, followed by a metallic Ni layer, a mixed FeNi alloy component, and an inner Cu core. As for the NiFeCo catalyst (Figure 2c), the outer layer comprises FeCoNi oxides, followed by a Ni-rich CoNi layer and an inner FeCo-enriched FeCoNi alloy core. Also, the NiFeMn catalyst presented significantly different layered structures than the other NiFeM catalysts (Figure 2d). Most Mn species are only located at the outside layer in the form of Mn oxide, followed by an intermediate layer of Ni metal and an inner FeNi alloy core. The various nanostructures and elemental distribution for each NiFeM catalyst are likely responsible for their OER activity measured in aqueous alkaline electrolyte and AEM-based water electrolyzer environments.

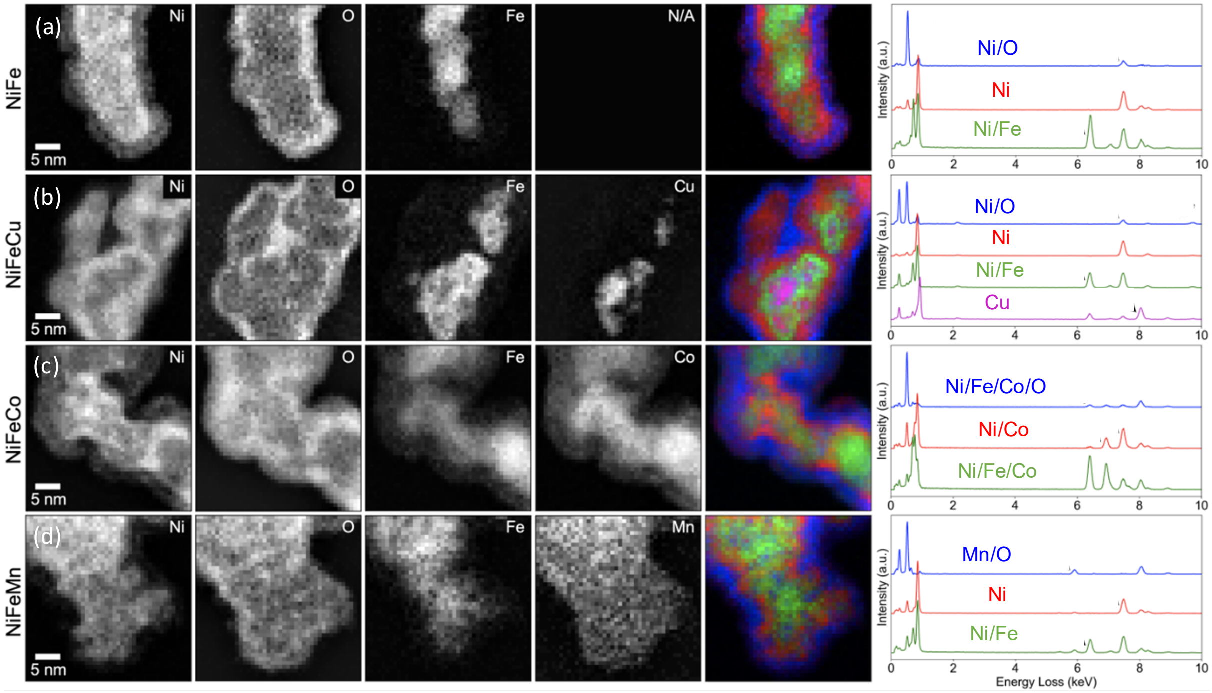

**Figure 2**. Comparison of the nanostructure and distribution of chemical compositions in NiFe and ternary NiFeM nanofoam catalysts by STEM-EDS. Each row shows results for an individual catalyst: (a) NiFe, (b) NiFeCu, (c) NiFeCo, and (d) NiFeMn. Grayscale maps show the distribution of individual elements. In contrast, the colored maps indicate regions with distinct compositions, mapped by multivariate curve resolution (MCR) analysis of the spectrum images, with the corresponding spectral components.

The formation of different layered structures and elemental distributions could be explained using the redox potentials of various metals (*i.e.*, Ni, Fe, Cu, Co, and Mn) used for ternary catalyst synthesis. In the case of the NiFeCu nanofoam, Cu ($Cu^{2+}/Cu = 0.337$ V *vs*. RHE) has a more positive redox potential than Fe ($Fe^{3+}/Fe = -0.04$ V) and Ni ($Ni^{2+}/Ni = -0.25$ V). Therefore, Cu precursors would be reduced first and entirely, forming the catalyst core. After the core is formed and the Cu precursors are consumed, the residual Ni and Fe precursors would be reduced to form the NiFe mixed-phase intermediate layer, followed by a Ni-enriched outermost layer because Ni has the highest concentration. Due to the hydrolysis process in water, part of the outermost Ni may be later converted to the amorphous $Ni(OOH)_2$, the OER intrinsic active sites.[30] As for the NiFeCo sample with a FeCo-rich core, Co ($Co^{2+}/Co = -0.28$ V) has a similar redox potential to Ni, so it is reasonable to accompany Ni in the outermost shell and second layer. As for the NiFeMn, Mn ($Mn^{2+}/Mn = -1.18$ V) has the most negative redox potential, which is challenging to reduce. Thus, it appears mainly in the shell. Unlike previously studied transition metal oxide catalysts suffering from insufficient electrical conductivity due to dominant metal oxide or oxyhydroxide, these NiFeM catalysts contain significant interconnected metallic crystalline cores, which can provide fast electron transfer. This is crucial for enhancing anode performance, especially in MEAs for AEMWE at high current densities ($>2.0$ $Acm^{-2}$).

X-ray diffraction (XRD) patterns were acquired to study the crystalline structures of these as-synthesized binary NiFe and trimetallic NiFeM nanofoam catalysts (Figure 3a). All samples exhibit one pronounced broad peak around $45^{o}$, indicating the formation of amorphous structures, consistent with the STEM image analysis.

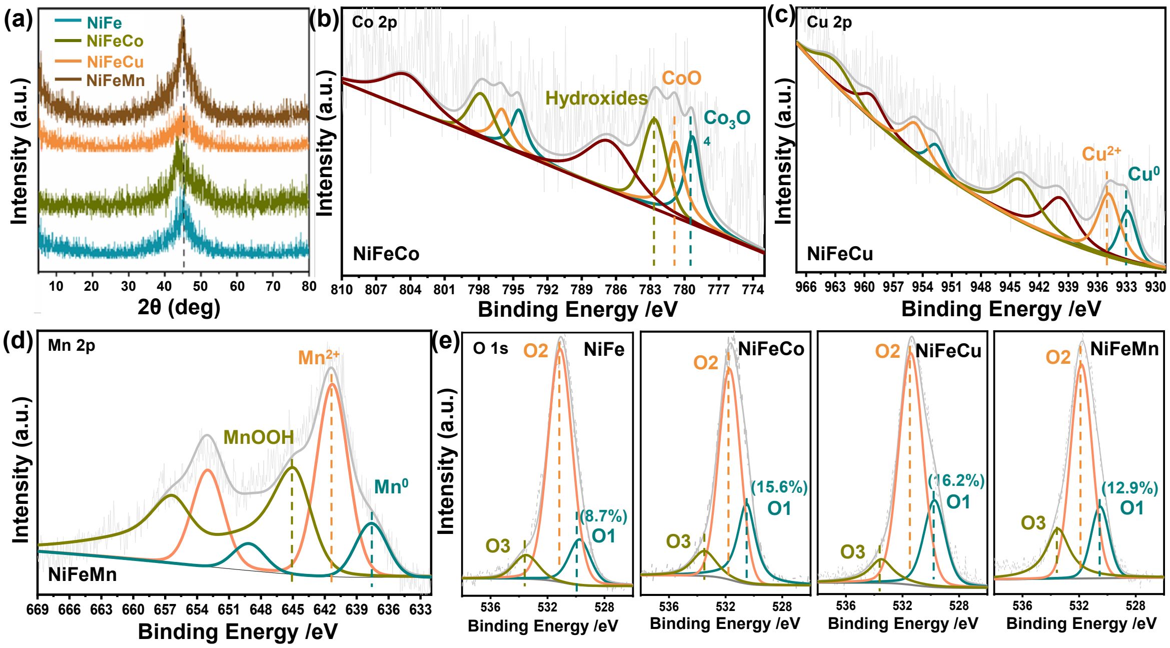

**Figure 3**. (a) XRD patterns, and (b-e) XPS analysis for as-synthesized trimetallic NiFeM catalysts, including (b) Co 2p, (c) Cu 2p, (d) Mn 2p, and (e) O 1s spectra.

Surface compositions were also studied by X-ray photoelectron spectroscopy (XPS), as presented in Figures 3b-e, Figure S4, and Table S2. The XPS spectra show the Ni 2p, Fe 2p, M 2p (M = Cu, Co, Mn), and O 1s peaks for the as-synthesized NiFe and trimetallic NiFeM nanofoams. The Ni 2p peaks in the XPS spectra for the NiFe nanofoam can be deconvoluted into metallic $Ni^0$ (852. 7 and 870.2 eV), oxidized $Ni^{n+}$ (856.3 and 874.0 eV), and satellite (861.5 and 880.1 eV) peaks (Figure S4a).[31, 32] As for the $Ni_2Fe_1M_{0.75}$ nanofoams, the prominent peaks of metallic $Ni^0$ and oxidized $Ni^{3+}$ show a slight shift to higher energies, suggesting the fine-tuning of the surface electronic structures of Ni. Similarly, the Fe 2p peaks for the $Ni_2Fe$ nanofoam can be deconvoluted into metallic $Fe^0$

(707.0 and 720.8 eV), oxidized $Fe^{3+}$ (711.0 and 724.8 eV), hydroxides (713.5 and 727.1 eV), and satellite (718.0 and 733.3 eV) peaks (Figure S4b). For the Fe 2p peaks in the $Ni_2Fe_1M_{0.75}$ nanofoams, the appearance of a $Fe^{2+}$ peak is significant, implying that the introduction of the third metal may change the electronic structure of the Fe phase. The Co 2p peaks for the $Ni_2Fe_1Co_{0.75}$ nanofoams are mainly composed of Co oxides, consistent with the STEM-EDS, which showed Co and O in the shell (Figure 3b). In contrast, for the Cu 2p peaks in $Ni_2Fe_1Cu_{0.75}$ nanofoams, Cu deconvoluted into primary metallic Cu and minor $Cu^{2+}$ (Figure 3c). For the Mn 2p peaks in $Ni_2Fe_1Mn_{0.75}$ nanofoams, Mn was deconvoluted into metallic Mn, oxidized Mn, and MnOOH (Figure 3d). The O 1s XPS for the various samples is compared in Figure 3e, which can be deconvoluted into three components: lattice oxygen (O1), mixed oxides/hydroxides (O2), and water adsorption for (O3), respectively.[33, 34] The lattice oxygen in the bulk oxide shell could modify the OER electron transfer mechanism and change the rate-limiting step toward OER *via* a pH equilibrium rather than a proton-electron transfer step.[35, 36] Among them, the $Ni_2Fe_1Cu_{0.75}$ nanofoam contains relatively higher O1 than the other samples. Therefore, NiFeCu is probably more pH-dependent than Co and Mn for OER catalysis through a non-concerted proton-electron transfer mechanism.

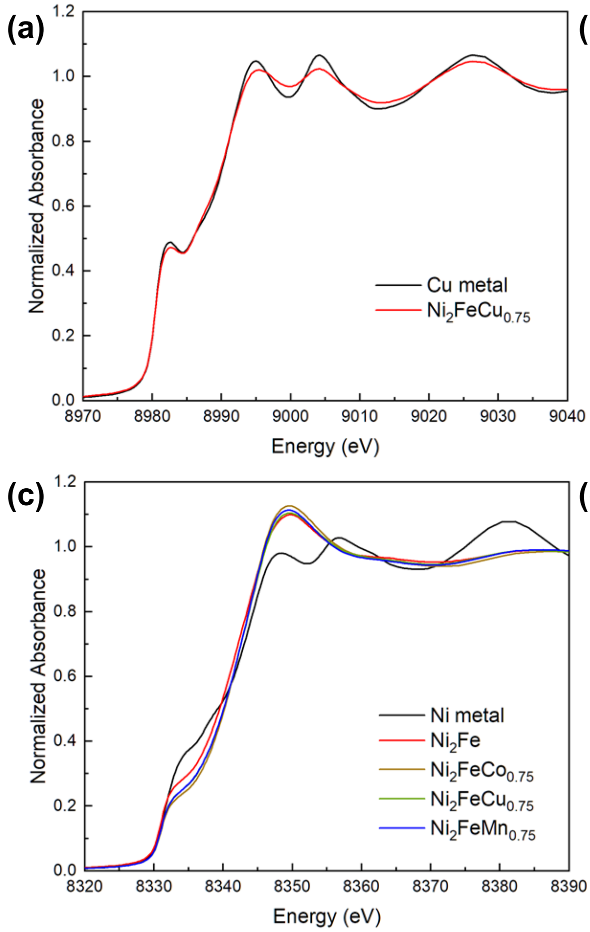

**Figure 4.** K edge XANES for NiFeM catalysts: (a) Cu, (b) Fe, (c) Ni, and (d) Co.

X-ray absorption fine structure (XAFS) spectra were measured at the Mn, Fe, Co, Ni, and Cu K edges (Figure 4 and Figures S5-S10). Of these, the Cu K edge of $N_1FeCu$ is the simplest to interpret due to the similarity of the XANES compared to a Cu foil standard (Figure 4a and Figure S5). The similarity of the pre-edge peak at 8982.5 eV indicates metallic copper, while the attenuated features at the absorption edge suggest metallic Cu nanoparticles. These features imply that almost all Cu is in *fcc* (face-centered cubic) metallic copper nanoparticles with little interaction with Ni or Fe. Fully coordinated bulk copper metal has 12 nearest neighbors. Quantitative fitting of the extended X-ray absorption fine structure (EXAFS) using a multi-shell, multiple-scattering model with minimal parameters reveals a Cu-Cu coordination number of 10.7 ± 0.3 (Table S5). Since surface atoms often have lower coordination, average coordination numbers can be correlated with particle size, which for Cu in NiFeCu corresponds to ~5 nm. If these particles were the cores of larger metallic particles, the Cu would be expected to be nearly fully coordinated, as observed. In contrast, similar metal-metal scattering associated with Ni or Fe is not observed with the NiFeCu catalysts and others due to the absence of significant features of a *fcc* structure in the XANES and beyond the nearest neighbor (Figures 4b-4c and Figures S6-7). The Cu nearest neighbor bond length is somewhat shorter than bulk copper, and the mean square relative displacement (MSRD), $\sigma^2$, also sometimes named the EXAFS Debye-Waller factor, is larger than bulk copper from EXAFS fit results: $\Delta R$ =-0.010 ± 0.005 Å, $\Delta\sigma^2$ = +0.0016 ± 0.0005 Å$^2$. Although all indications are consistent with predominantly metallic Cu nanoparticles, XAFS cannot preclude a small amount of alloying. This is consistent with the EDS mapping and XPS analysis and would provide excellent electrical conductivity for the OER.

From Mn XANES (Figure S8), Mn in FeNiMn is predominantly in the 2+ oxidation state, consistent with the multiple oxide and oxyhydroxide phases observed by XPS, but with no evidence of metallic Mn, which may be a small fraction that is observed by XPS due to the surface sensitivity of XPS. This agrees with the STEM-EDS observations, which indicated only a small amount of Mn in the outer shell. This also agrees with the previous discussion that Mn is the most challenging to reduce to a metallic state due to the most negative potential.

All the other XANES spectra (Fe, Ni, Co) exhibit a mixture of metallic and oxide characters (Figure 4b-4d and Figures S9-S10). EXAFS fits indicate that the oxide-to-metal ratio is highest for nickel, while the ratios for Fe and Co are lower (Tables S3-S6). The Fe XAFS for NiFe and NiFeMn exhibits *bcc* features. A peak in $\chi(k)$ at $k$=5.3 $Å^{-1}$ corresponds to a feature in Fe metal (*bcc*) that is only present with the longer range order beyond 3.4 Å (Figure S6). Consequently, the Fourier transform shows a similar structure between 3.4 and 6 Å for NiFe, NiFeMn, and Fe metal. Given these indicators and the similarity of the NiFe and NiFeMn spectra, we have fit the Fe EXAFS by constraining the Fe-$M_{bcc}$ paths to be the same length and assuming the same ratio of shorter to longer path coordination number for both spectra (Table S4). Including Fe-$M_{bcc}$ significantly increased the fit quality, decreasing the reduced-$\chi^2$ for the simultaneous fit from 8312 to 5861 eV and the individual R factors from 1.5 to 0.3% and 0.7 to 0.3%, for NiFe and NiFeMn, respectively. The Ni K edge spectra do not exhibit the same *bcc* features as Fe, which suggests some metallic phase segregation.

Except for the two Fe spectra for NiFe and NiFeMn, the other Fe, Ni, and Co edge spectra are atypical, as the XANES does not match the bulk metal foils and the EXAFS exhibits little structure above 4 Å, a region where one typically sees characteristic metal-metal scattering peaks in nanoparticles.[37, 38] Specifically, they do not have *fcc* or *bcc* features near the absorption edge or in the Fourier transform. Even considering the M-O paths, the M-M coordination numbers are low, which may be interpreted as a very small average particle size or a defective structure. The similarity at all three edges for the NiFeCo catalyst implies that these metals are well mixed in the particles. In contrast, Cu phases are separated in the NiFeCu sample, and the presence of Cu inhibits the *bcc* Fe phase, giving rise to more intimately mixed NiFe.

The model for fitting the Ni edge was improved by including the third cumulant ($C_3$), the first asymmetric component of the mathematical expansion of the path length distribution. According to fitting results, a modest decrease in the R factors, higher MSRD ($\sigma^2$), and utility of $C_3$ suggest defective structures, which could indicate a glassy or amorphous metallic Ni phase in all samples.

## 2.2. Half-cell OER activities in alkaline electrolytes

Currently, FeNi-based catalysts are considered state-of-the-art PGM-free OER catalysts in alkaline media.[39, 40] Introducing a third metal to the NiFe catalyst could further modify the adsorption energy of the intermediate on NiFe catalysts by shifting the $Ni^{2+}/Ni^{3+}$ redox peaks.[36, 41-43] Here, Co, Cu, or Mn elements were added to the NiFe phase to design trimetallic NiFeM catalysts for further performance improvement, especially in MEAs for actual AEMWEs. To assess their OER activities, these NiFeM catalysts with different M/Fe ratios were first tested with a fixed and optimal Ni to Fe ratio of 1:2 (Figure S11). Various compositions of the best-performing NiFeM catalysts are displayed in Figure 5a, where NiFe nanofoam and commercial $IrO_2$ are also included for a comparison. As exhibited in Figure 5b, introducing Co decreases the overpotential and improves the OER current density in the higher potential range. Cu and Mn could also significantly increase the current density in the higher potential region. Furthermore, introducing Co increases the reaction kinetics by analyzing their Tafel slopes in Figure 5c. The above analysis indicated that the OER activity improvement of the NiFeCo electrocatalyst related to traditional NiFe catalysts is remarkable, which was further compared with the reported electrocatalysts, showing superior OER activity in alkaline media (Table S7).

In contrast, the Cu and Mn-containing NiFe catalysts show slower reaction kinetics in the smaller overpotential range. However, these catalysts favor a faster electron transfer rate that offsets the current density loss at a higher potential, possibly due to the modification of the electronic structures of Ni and Fe components as evidenced in the XPS of Ni and Fe peaks, and the enhancement of electrical conductivity in the catalysts. Multi-step current density tests of the NiFeM and $IrO_2$ catalysts were compared using the amperometric *i-t* technique at 1.9 V in a homemade two-electrode H-cell (Figure S11e). The multi-current step test in Figure 5d indicates that compared with $IrO_2$, the NiFeM exhibits a relatively smaller potential increase as the current density rises. SEM and TEM images of the NiFeCo catalyst after 100-hour stability testing (Figure S12) demonstrated that the catalyst maintains the original morphology and porosity, indicating structural stability (Figure S13).

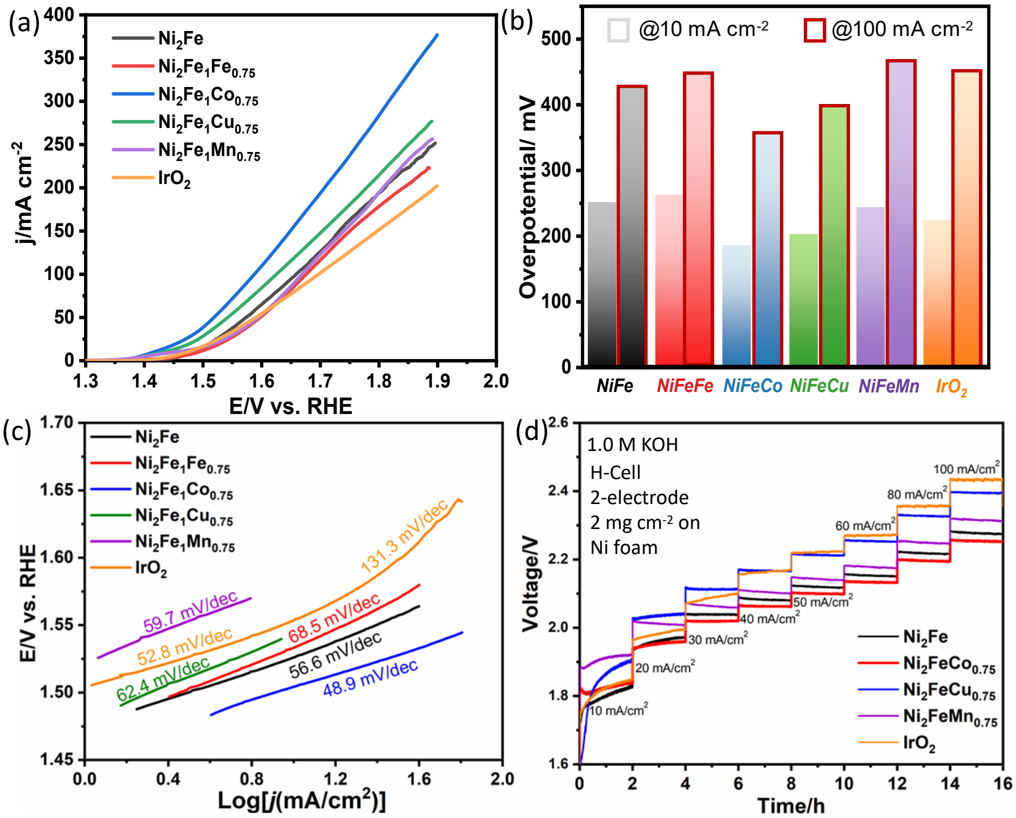

**Figure 5.** The measured OER activity and stability of the studied NiFe and NiFeM nanofoam catalysts. (a) LSV curves of $Ni_2Fe_1M_{0.75}$ samples and $IrO_2$ were recorded on a RDE using three-electrode systems in $O_2$-saturated 1.0 M KOH at a scanning rate of 5 mV s$^{-1}$, rotating rate of 1600 rpm, and mass loading of 0.32 mg cm$^{-2}$. (b) OER overpotentials at 10 and 100 mA cm$^{-2}$. (c) Corresponding OER Tafel plots on studied catalysts. (d) Multi-step current density test using H-cell with a two-electrode system loading 2 mg cm$^{-2}$ anode catalysts in 1.0 M KOH as shown in Figure S11e.

### 2.3. DFT calculations to elucidate the promotional role of the third metal

To reveal the role of the third element in the improved performance of the ternary NiFeM catalysts relative to binary NiFe catalysts, we performed DFT calculations for the most intrinsically active NiFeCo catalysts. NiFeCo oxyhydroxides were constructed by doping Co on the surfaces of γ-NiFe LDH hosts (Figure 6a). Based on the calculated surface phase diagrams (Figure 6b and Figure S14), similar to NiFe LDH and other Ni-based LDHs,[52, 53] surface metal sites of NiFeCo are saturated with OH by forming atop OH. However, surface O sites are saturated with H adsorption by forming bridge OH. Thus, OER on the ternary NiFeCo does not go through the traditional Langmuir-Hinshelwood mechanism that starts from the adsorption of reaction intermediates but goes through the Mars van Krevelen mechanism starting from the redox of surface species, *i.e.*, the oxidation of OH* to O*. OER further proceeds by forming OOH*, $O_2$ + surface vacancies, and OH adsorption at the vacancies to close the cycle. Also, we found that deprotonation of OH* to O* is the potential limiting step, and the reactions starting from bridge OH* are more favorable than atop OH* (Figure S15-S21). Such a preference suggests that dual-metal sites are reaction centers.

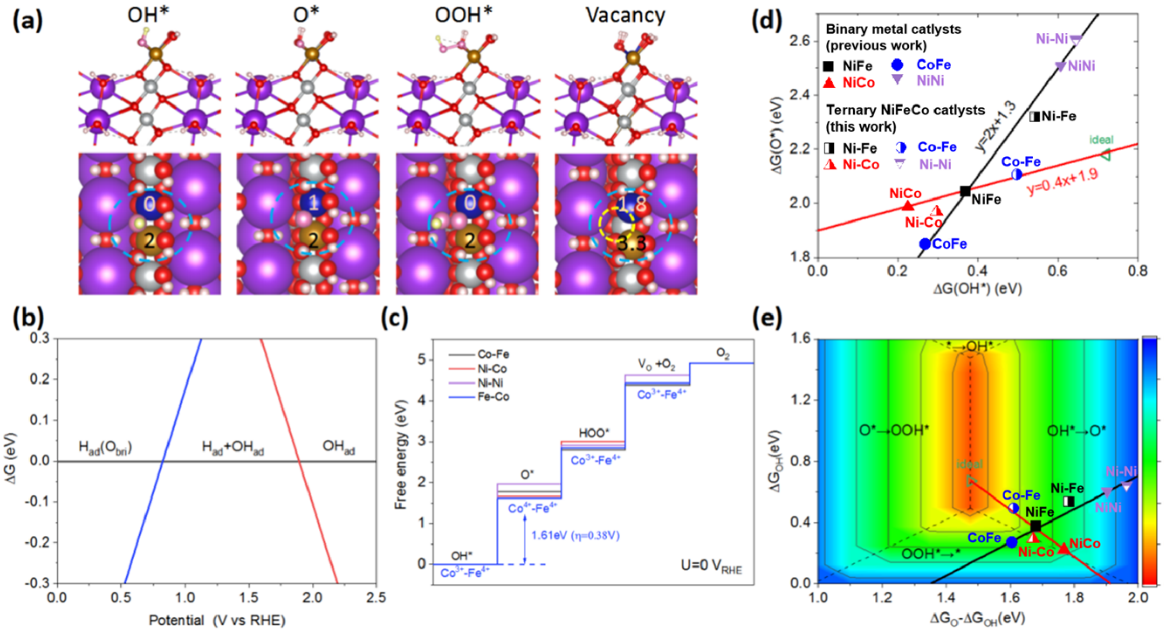

**Figure 6.** OER mechanism and reaction centers on ternary NiFeCo catalysts. (a) Structures of OER intermediates; adsorbate atoms are differentiated from catalysts by colors (yellow instead of white for hydrogen and rose instead of red for oxygen, respectively). A yellow circle indicates the formation of a surface O vacancy. Light blue circles highlight the reaction centers on the top views. The magnetic moments of Co and Fe during OER are also given on the top views. (b) Surface phase diagram of NiFeCo catalysts. (c) Reaction free-energy diagrams of dual metal sites for OER on ternary NiFeCo catalysts. The potential limiting steps and the overpotentials are also given for the Co-Fe center. The oxidation states are given based on the intrinsic magnetic moments (**Table S8**). (d) Scaling relationship between OH* and O* intermediates at the reaction centers. (e) Two-dimensional (2D) Volcano plot of the OER overpotential as a function of Gibbs free energies of the reaction intermediates. We also include the data points of some binary catalysts from previous work as a comparison.

Co-doping leads to four reaction centers on ternary NiFeCo surfaces, including Ni-Fe, Co-Fe, Ni-Co, and Ni-Ni dual metal sites. The overpotentials ($\eta$) of the OER on each reaction center were calculated to be 0.54 V (Ni-Fe), 0.38 V (Co-Fe), 0.44 V (Ni-Co), and 0.74 V (Ni-Ni) (Figure 6c). Among them, the overpotential of the Co-Fe center is 70 mV lower than that of binary NiFe catalysts,[32, 53] which explains the enhanced intrinsic activity of ternary NiFeCo catalysts than binary NiFe. Generally, there are two reasons for the improved activity of Co-Fe centers of NiFeCo in comparison with binary NiFe catalysts. The first reason is that the structural and electronic-structural perturbation induced by the third element leads to fine-tuning the redox ability of the metal sites at the reaction centers. Specifically, such a perturbation makes the redox of $Co^{3+}$ in the NiFeCo catalyst more flexible than in their binary counterparts, while the trend is the opposite for both $Fe^{4+}$ and $Ni^{3+}$. As characterized by the change of Co magnetic moment from 0 to $1\mu_B$, the potential limiting step of bridge OH ($Co^{3+}$-OH-$Fe^{4+}$ and $Ni^{4+}$-OH-$Co^{3+}$) deprotonation to form bridge O ($Co^{4+}$-O-$Fe^{4+}$ and $Ni^{4+}$-OH-$Co^{4+}$) is accompanied by $Co^{3+}$ oxidation to $Co^{4+}$. Such a redox at the Co-Fe and Ni-Co centers on the ternary NiFeCo are 0.1 and 0.19 eV more favorable than binary CoFe and NiCo catalysts, respectively. On the other hand, bridge OH deprotonation to form bridge O at the Ni-Fe center and accompanied oxidation of $Fe^{4+}$ to $Fe^{5+}$ is 0.09 eV less favorable on ternary NiFeCo than on binary NiFe catalysts. Consequently, Co-Fe dual sites on the NiFeCo catalyst become more active than the Ni-Fe sites on both the ternary NiFeCo catalyst and the binary NiFe catalysts.

The second reason is that the dual-site synergy at the reaction center provides opportunities for breaking scaling relationships, as shown in Figure 6d. The OH-O scaling relationship of binary NiFe and CoFe follows the ideal slope of 2, which implies the limited potential for further improvement of OER activity if all catalysts follow such a scaling relationship. However, a recent study suggested that forming binary metal oxyhydroxides with dual metal sites at the reaction centers or introducing a third element into NiFe can break OH-O scaling. Such a hypothesis is confirmed in the current work, *i.e.*, both Ni-Co and Co-Fe dual sites on NiFeCo catalysts follow a scaling relationship with a slope of 0.4, which significantly deviates from the ideal value (*i.e.*, 2). While breaking OH-O scaling does not necessarily lead to catalysts with improved OER activity (*e.g.*, Ni-Co dual sites on the NiFeCo catalysts), it does provide the direction for such a possibility. That weakens the OH binding energy compared to binary NiFe catalysts. Such a weakening is precisely the case of the Co-Fe center on the ternary NiFeCo, for which OH adsorption is weakened 0.13 eV, compared to binary NiFe catalysts. Consequently, Co-Fe centers become closer to the maximum of the 2D volcano, in contrast to Ni-Fe centers (Figure 6e).

Thus, introducing a third element into NiFe and potentially other binary catalysts is a proven strategy to enlarge the design space of oxyhydroxide catalysts with OER activity beyond the state-of-the-art NiFe-based catalysts by breaking the OH-O scaling relationship.

### 2.4. MEA Performance in AEMWEs using diluted KOH and pure water

To further evaluate studied NiFeM anode catalysts in AEMWEs, we integrated these NiFe and NiFeM anode catalysts with commercially available ionomers and AEMs to fabricate MEAs at Giner Inc. The resulting PGM-free anode-based MEAs were compared with the $IrO_2$ anode under various testing conditions by flowing 0.1 M KOH solution (Figures 7a-b) and pure water (Figures 7c-d) on the anode. In the case of 0.1 M KOH solution, when applied voltages are below 1.5 V, the $IrO_2$ anode demonstrated slightly higher performance than NiFeM-based samples. In contrast, at voltages higher than 1.5 V, these NiFeM-based materials showed significant advantages in generating higher current densities than the $IrO_2$ anode, agreeing with the RDE tests in aqueous concentrated KOH electrolytes. As for NiFe-based PGM-free anode, the continuous conversion of metals to metal oxyhydroxides at higher voltages could remarkably increase the number of active sites and favor $OH^-$ transfer, thus accelerating the reaction process. Notably, the ternary $Ni_2FeMn_{0.5}$ catalyst exhibits the highest current density of 2.0 A $cm^{-2}$ when holding a constant voltage at 1.7 V, followed by $Ni_2FeCu_{0.5}$, $Ni_2FeCo_{0.5,}$ and $Ni_2Fe$, whereas all the catalysts have similar area-specific high-frequency resistance (HFR) values (Figure S22). In addition, similar performance of $Ni_2FeMn_{0.5}$ can be observed in the range of batch reproducibility (Figures S23-S24). The detailed comparison between $Ni_2FeMn_{0.5}$ and other OER electrocatalysts in AEMWEs is shown in Table S9. The excellent MEA performance of $Ni_2FeMn_{0.5}$ is possibly derived from the $Mn^{2+}$ doping into the surface Ni(OOH) layer with a body-centered cubic structure, as evidenced by XAFS, resulting in optimization of the electronic structure.[54] These ternary NiFeM catalysts do not present similar performance trends between concentrated KOH electrolytes and actual AEMWEs using diluted 0.1 M KOH (Figure S25). The likely reason is the different behaviors of studied NiFeM OER catalysts under more complex operating conditions in AEMWEs. For example, the MEA tests depend on the interface resistance, electron/$OH^-$ conductivities and ionomer conductivity, and mass transfer through the catalysts. In addition, the *in-situ* formed metal oxide/oxyhydroxide under

AEMWE conditions may have different chemical, morphological, and structural properties, showing inconsistent performance compared to half-cell tests using concentrated KOH.

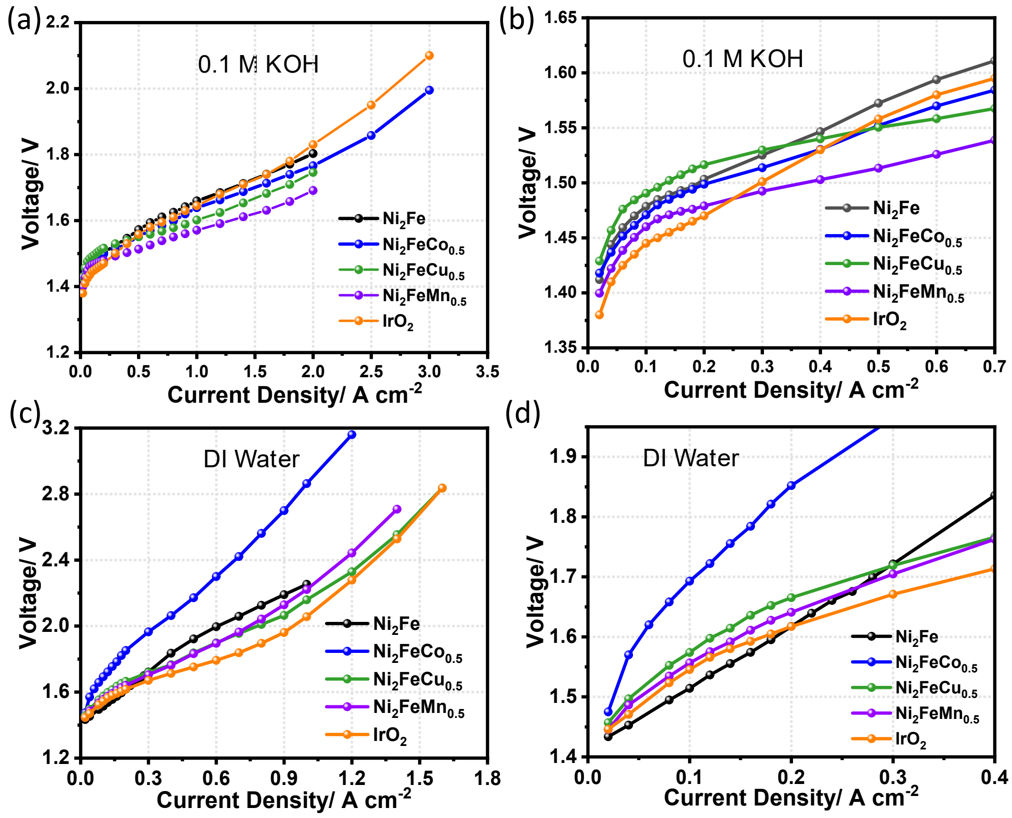

**Figure 7.** MEAs performances and the zoom-out area in the low voltage range by flowing with (a, b) 0.1 M KOH and (c, d) pure de-ionized water, respectively. The loading of the studied anode catalysts, including PGM-free and $IrO_2$, is 3 mg cm$^{-2}$. PtRu/C catalysts with a loading of 1 mg cm$^{-2}$ were used to minimize the effect of the cathode. The active cell area is 5 cm$^2$. The AEM (80 $\mu$m) and ionomers are from *Versogen*. The tests were conducted under ambient pressure at 80 $^{o}$C for pure water and 0.1 M KOH with a flow rate of 0.35 mL min$^{-1}$ (700 mA at 1.85 V).

Furthermore, we investigated these NiFeM anodes in AEMWEs by flowing pure water, which is more desirable for practical applications in renewable energy conversion devices.

As shown in Figures 7c-d, the $Ni_2Fe_1Cu_{0.5}$ catalyst performed better than the other ternary $Ni_2Fe_1M_{0.5}$ and the binary $Ni_2Fe$ catalysts and delivered comparable performance to $IrO_2$, generating a current density of 1.2 A $cm^{-2}$ at ~2.3 V. The four-layered structure of the $Ni_2Fe_1Cu_{0.5}$, with a stable metallic Cu core, may facilitate faster electron-donating features in promoting the four-electron transfer process and provide efficient $OH^-$ transfer during the OER reaction in AEMWEs with pure water. Also, these NiFeM catalysts behave differently in AEMWEs when using diluted KOH solution compared to pure water, which is likely because the real active sites and surface layer morphologies during the OER are greatly dependent on surface pH values, working temperature, and $OH^-$ conductivity in ionomer. The stability of PGM-free anode in AEMWEs was studied with pure DI water and 0.1 M KOH at 0.5 $Acm^{-2}$ (Figure S26). Regardless of the $Ni_2Fe$ and $Ni_2FeCu$ anodes, these catalysts remain stable after 24 hours of continuous operation at 0.5 $Acm^{-2}$ in 0.1 M KOH, compared with rapid decay in DI water. The morphological and structural changes of NiFeM electrocatalysts after durability tests were further investigated. There is no apparent change in the electrode's shape, morphology, nanostructure, and distribution after 100 hours of testing (Figure S27). After the stability test, the catalyst can retain its porous network morphology, indicating its chemical and mechanical ability to withstand the oxidation and effects of $O_2$ bubble formation and the pressure stresses within the anode during the OER.

Generally, compared with the binary $Ni_2Fe$, the improved AEMWE performance of the $Ni_2FeM$ anodes was attributed to the enhanced intrinsic OER activity due to optimal electronic properties of surface oxides *via* adding the third metal, enhanced electrical conductivity of the metallic core, and favorable mass transport within nanofoam morphologies. However, the exact mechanism and actual active site structures need further investigation using advanced Operando spectroscopy. Notably, the encouraging performance of these PGM-free ternary NiFeM anode catalysts in AEMWEs, regardless of using pure water or dilute KOH solution, further confirms their feasibility for hydrogen generation *via* clean and low-cost AEMWEs. In particular, using a diluted KOH electrolyte, the studied ternary NiFe M anode demonstrated encouraging performance and durability simultaneously in AEMWE. However, exploring high-performance and durable AEMWEs using more desirable pure water still faces significant challenges due to the unstable catalyst/electrolyte interfaces and increased HER during the long-term operation.

## 3. Conclusions

In summary, by regulating the third metal and incorporating it into current NiFe catalysts, we developed a variety of porous and multilayered ternary NiFeM (M: Co, Cu, or Mn) network nanofoam OER catalysts with unique amorphous oxide shells and crystalline mix-phased metallic glass core structures. These catalysts were successfully implemented in MEAs for AEM-based water electrolyzers. Unlike traditional metal oxide catalysts, the new ternary NiFeM catalysts feature unique metallic glass structures and a multiple-layered core-shell configuration, demonstrating excellent electrical conductivity and significantly enhanced electrolyzer performance compared to traditional binary NiFe catalysts. Introducing a third transition metal element can generate a more active dual metal site, such as Co-Ni and Co-Fe, which could reduce the energy barrier of the potential limiting step associated with the conversion of OH to O during the OER. In addition, the synergy of dual metal sites could break OH-O scaling during the OER, providing optimal adsorbing energy for these critical intermediates. Furthermore, the inner crystalline core contributes significantly by promoting the electron-donating process, accelerating the reaction, especially in water electrolyzers operating at high current densities. Besides benefiting from the self-supported and meso- and macro-porous structure, these 3D metallic glassy catalysts have high corrosion resistance at a higher potential, significantly alleviating the corrosion issues when using carbon-based OER catalysts.

Among the catalysts studied, the NiFeCo exhibited the best catalytic activity and stability for the OER, determined using a half-cell with concentrated aqueous alkaline electrolytes. In contrast, the NiFeMn catalyst delivered a remarkably enhanced current density of 2.0 A $cm^{-2}$ at 1.7 V in an AEM-based MEA, superior to the $IrO_2$ reference, when 0.1 M KOH solution was supplied to the anode. Furthermore, the NiFeCu catalyst generates a very encouraging current density of 1.2 A $cm^{-1}$ at the voltage of ~2.3 V when pure water is used, also approaching the $IrO_2$ reference anode, especially at high current densities. These NiFeM catalysts behave differently under various environments for the OER, further highlighting the complexity of understanding the actual active sites, catalyst/electrolyte interfaces, and real surface morphologies/structures of anode catalysts during the OER. This will require advanced operando experiments to provide insights into the origin of catalytic properties under different environments.

Meanwhile, it should be noted that well-defined AEMWE testing conditions are crucial to evaluating studied OER catalysts, such as temperature, electrolyte concentrations, ionomer/AEM, catalyst loading, and operating voltages. Importantly, due to the dynamic changes in catalyst structures and morphologies, achieving a steady state OER on studied catalysts is necessary for recording reliable performance.

Given the encouraging MEA performance achieved in actual AEMWEs, adding the third metal to design and engineer optimal NiFeM catalysts with optimal electronic and geometric structures effectively improves the performance of current NiFe catalysts. It is crucil for eventually replacing expensive PGM anode materials, *i.e.*, $IrO_2$, for low-cost and viable water electrolyzers.

## 4. Experimental Section

*Synthesis of NiFeM nanofoam catalysts:* The synthesis method is modified from a one-step co-reduction strategy. Taking the optimal $Ni_2FeCo$ synthesis as an example, 0.2 M $NiCl_2$, 0.1 M $FeCl_3$, and 0.1 M $CoCl_2$ were quickly mixed into a vial containing 10 mL DI water, followed by a quick injection of 5 mL 0.1 M $NaBH_4$ aqueous solution. The reaction will take about 5 minutes under stirring until the upper solution becomes colorless. Then, the precipitates could be collected by vacuum filtering or centrifuge at least three times, followed by a freeze-drying process. Synthesis of other tri-metallic NiFeCu and NiFeMn nanofoams with different metal ratios follow similar procedures except for changing the third metal precursors and their concentrations accordingly.

*Materials characterization:* The scanning electron microscopy (SEM) images were acquired on a Hitachi SU 70 microscope at a working voltage of 5 kV to study the overall morphology of NiFeM catalysts. Furthermore, the nanoscale structure and composition of the catalysts were studied by scanning transmission electron microscopy (STEM) and energy dispersive X-ray spectroscopy (EDS) in the Center for Nanophase Materials Sciences at Oak Ridge National Laboratory. STEM experiments were performed on a JEOL JEM-ARM200F (NeoARM) instrument equipped with an integrated ASCOR (Cs) probe corrector and two JEOL DrySD 100GV EDS detectors. X-ray absorption spectroscopy experiments were carried out at beamline 10-BM at the Advanced Photon Source (APS/10-BM), Argonne National Laboratory. Specimens were prepared as self-supporting pellets and measured in transmission mode at the Mn, Fe, Co, Ni, and Cu K edges. Edge steps (x) ranged from 0.35 to 1.10. Harmonics were reduced by detuning the second crystal to 50% of the peak intensity. Reference spectra of metal foils were measured simultaneously for all but the Mn edge and calibrated to the zero-crossing of the second derivative for the corresponding metal foil (Fe: 7110.75 eV; Co: 7708.78 eV, Ni: 8331.49 eV, Cu: 8980.48 eV). Spectra were processed and fit using the *Demeter/Athena/Artemis* suite of XAFS analysis software[55] and the EXAFS scattering paths were calculated using *feff* version 6.[55] A single correct Eo value cannot be selected, even in principle, for the mixed metallic and oxide species. Therefore, a somewhat arbitrary $E_0$ was selected for each element when extracting $\chi(k)$ from $\mu(E)$ so that the same $\Delta E_0$ could be used to simultaneously fit the Fe or Ni data sets. The $E_0$ energy selected for background removal and conversion to $k$ were 7112, 7709, 8333, and 8979 eV for Fe, Co, Ni, and Cu, respectively.

*Electrochemical measurement:* Catalysts ink preparation follows a typical procedure. For example, 1.0 mg NiFeM-based electrocatalyst powder was added into a vial, followed by 0.99 mL IPA and 10 μL Nafion. The homogeneous ink solution was obtained by ultrasonication for one hour. Next, catalyst ink was drop-cast onto a rotating disc to reach an optimal loading of 0.32 mg/cm$^2$. Electrochemical measurements were performed using a CHI760b electrochemical workstation coupled with a three-electrode cell system. A graphite rod and a saturated calomel electrode were used as the counter and reference electrodes, respectively. The reference electrode was calibrated to a reversible hydrogen electrode (RHE) by bubbling with pure hydrogen in the same electrolyte using a Pt wire coated with Pt black as the reference. During the measurement, cyclic voltammetry (CV) curves were conducted in $O_2$-saturated 1.0 M KOH aqueous solution between 1.2 and 1.9 V (*vs*. RHE) with a rotating rate of 200 rpm with a scan rate of 50 mV $s^{-1}$. Then, linear sweep voltammetry (LSV) curves were recorded between 1.2 and 1.9 V (*vs*. RHE) with a rotating rate of 1600 rpm at a scan rate of 5 $mVs^{-1}$ in $O_2$ saturated 1.0 M KOH aqueous solution.

*Two-electrode system test:* The multi-potential step tests were conducted in an H-cell employing a two-electrode system (Figure S11e). The HER cathode and the OER anode were made by spray coating PtRu/C and NiFeM catalysts onto Ni foam with a loading of 2 $mgcm^{-2}$, respectively.

*Membrane Electrode Assembly (MEA) fabrication and AEM electrolyzer tests:* The cathode electrode is made by spray coating 1.0 $mg_{Pt}cm^{-2}$ (PtRu/C) on Freudenberg H23C6 gas diffusion layer (GDL). The anode electrode is made by coating 3 mg $cm^{-2}$ NiFeM catalysts on Platinized Titanium layer (PTL). The loading of the reference $IrO_2$ is 2-3 mg $cm^{-2}$. The cathode catalysts ink contains 9.5 wt% ionomers, while the anode catalysts ink contains 20 wt% ionomers. The ionomer is TP85 5 wt.% ionomer dispersed in ethanol. The 80 $\mu$m thick AEM membrane from *Versogen,* anode, and cathode electrodes, Teflon gaskets were assembled into an area of 5 $cm^2$ single cell with 60 inch-pounds torque. The cell was tested by monitoring the voltage with a power booster. The cell was first held at 0.1 $Acm^{-2}$ using 0.1 M KOH aqueous solution until the voltage stabilized at 80 $^{o}$C. The polarization curve was recorded with a current density range between 0-3.5 $Acm^{-2}$. Then, the alkaline solution was purged with water at a current density of 0.1 A/$cm^2$ until the voltage was stabilized. The polarization curves were recorded with a current density between 0-1.6 A/$cm^2$.

**Supporting Information**

Supporting Information is available from the Wiley Online Library or from the author.

**Acknowledgements**

The authors are grateful for the financial support from U.S. Department of Energy, Hydrogen and Fuel Cell Technologies Office. STEM and EDS research was supported by the Center for Nanophase Materials Sciences (CNMS), which is a U.S. Department of Energy, Office of Science User Facility at Oak Ridge National Laboratory. The X-ray absorption (MRCAT, 10-BM, and 10-ID) experiments were performed at the Advanced Photon Source (APS), a DOE Office of Science User Facility operated for the DOE Office of Science by Argonne National Laboratory under Contract No. DE-AC02-06CH11357. The operation of MRCAT at the APS is supported by the Department of Energy and the MRCAT member institutions. The submitted manuscript has been created, in part, by employees of UChicago Argonne, LLC, Operator of Argonne National Laboratory under Contract No. DE-AC02-06CH11357.

**Conflicts of interest**

There are no conflicts to declare.

**Author Contributions**

X. Y., J. L., Q. S., and M. J. Z. contributed equally to this work. G.W., Q. S., and X. Y. conceived catalyst design and synthesis concepts. X.Y., Q.S., B.S., H.Z., and J.L. carried out catalyst synthesis, characterization, electrochemical measurement, and data analysis and interpretation. M.J. Z. performed electron microscopy analysis. S.K., M.P., N.M., D.S., Y.Y., and H.X. conducted

MEA fabrication, tests, and data analysis for AEM water electrolyzers. J.Z., J.L., and Z.Z. carried out the theoretical calculations. A.J.K and D.J.M performed XAS analysis and data fitting. X.Y., Q.S., and G.W. wrote the paper. G.W supervised the execution of the overall project.

## Data Availability Statement

The data that support the findings of this study are available from the corresponding authors upon reasonable request**.**

**Keywords**

Alkaline water electrolyzers, hydrogen generation, oxygen evolution reaction, PGM-free electrocatalysts, core-shell structures

Received: ((will be filled in by the editorial staff))
Revised: ((will be filled in by the editorial staff))
Published online: ((will be filled in by the editorial staff))

## References

[1] Q. Shi, C. Zhu, D. Du, Y. Lin, *Chemical Society Reviews* **2019**, *48*, 3181.

[2] R. Abbasi, B. P. Setzler, S. Lin, J. Wang, Y. Zhao, H. Xu, B. Pivovar, B. Tian, X. Chen, G. Wu, *Advanced Materials* **2019**, *31*, 1805876.

[3] I. Vincent, D. Bessarabov, *Renewable and Sustainable Energy Reviews* **2018**, *81*, 1690.

[4] Y. Jiao, Y. Zheng, M. Jaroniec, S. Z. Qiao, *Chemical Society Reviews* **2015**, *44*, 2060.

[5] N.-T. Suen, S.-F. Hung, Q. Quan, N. Zhang, Y.-J. Xu, H. M. Chen, *Chemical Society Reviews* **2017**, *46*, 337.

[6] C. Zhu, Q. Shi, S. Feng, D. Du, Y. Lin, *ACS Energy Letters* **2018**, *3*, 1713.

[7] Q. Shi, C. Zhu, H. Zhong, D. Su, N. Li, M. H. Engelhard, H. Xia, Q. Zhang, S. Feng, S. P. Beckman, *ACS Energy Letters* **2018**, *3*, 2038.

[8] Q. Shi, C. Zhu, D. Du, J. Wang, H. Xia, M. H. Engelhard, S. Feng, Y. Lin, *Journal of Materials Chemistry A* **2018**, *6*, 8855.

[9] A. Zagalskaya, V. Alexandrov, *ACS Catalysis* **2020**, *10*, 3650.

[10] S. Fu, J. Song, C. Zhu, G.-L. Xu, K. Amine, C. Sun, X. Li, M. H. Engelhard, D. Du, Y. Lin, *Nano Energy* **2018**, *44*, 319.

[11] R. Chen, S. F. Hung, D. Zhou, J. Gao, C. Yang, H. Tao, H. B. Yang, L. Zhang, L. Zhang, Q. Xiong, *Advanced Materials* **2019**, *31*, 1903909.

[12] M. Asnavandi, Y. Yin, Y. Li, C. Sun, C. Zhao, *ACS Energy Letters* **2018**, *3*, 1515.

[13] M. Gong, H. Dai, *Nano Research* **2015**, *8*, 23.

[14] B. M. Hunter, H. B. Gray, A. M. Muller, *Chemical reviews* **2016**, *116*, 14120.

[15] M. W. Louie, A. T. Bell, *Journal of the American Chemical Society* **2013**, *135*, 12329.

[16] H. Koshikawa, H. Murase, T. Hayashi, K. Nakajima, H. Mashiko, S. Shiraishi, Y. Tsuji, *ACS Catalysis* **2020**, *10*, 1886.

[17] D. Li, E. J. Park, W. Zhu, Q. Shi, Y. Zhou, H. Tian, Y. Lin, A. Serov, B. Zulevi, E. D. Baca, *Nature Energy* **2020**, *5*, 378.

[18] M. Carmo, R. C. Sekol, S. Ding, G. Kumar, J. Schroers, A. D. Taylor, *ACS nano* **2011**, *5*, 2979.

[19] Y. Tan, F. Zhu, H. Wang, Y. Tian, A. Hirata, T. Fujita, M. Chen, *Advanced Materials Interfaces* **2017**, *4*, 1601086.

[20] R. Jiang, Y. Da, Z. Chen, X. Cui, X. Han, H. Ke, Y. Liu, Y. Chen, Y. Deng, W. Hu, *Advanced Energy Materials* **2022**, *12*, 2101092.

[21] F. Pan, Z. Li, Z. Yang, Q. Ma, M. Wang, H. Wang, M. Olszta, G. Wang, Z. Feng, Y. Du, *Advanced Energy Materials* **2021**, *11*, 2002204.

[22] Z. Liu, G. Wang, X. Zhu, Y. Wang, Y. Zou, S. Zang, S. Wang, *Angewandte Chemie International Edition* **2020**, *59*, 4736.

[23] H. Sun, Z. Yan, F. Liu, W. Xu, F. Cheng, J. Chen, *Advanced Materials* **2020**, *32*, 1806326.

[24] Y. Li, H. Zhang, M. Jiang, Q. Zhang, P. He, X. Sun, *Advanced Functional Materials* **2017**, *27*, 1702513.

[25] L. Xie, X. Li, B. Wang, J. Meng, H. Lei, W. Zhang, R. Cao, *Angewandte Chemie* **2019**, *131*, 19059.

[26] C. Niether, S. Faure, A. Bordet, J. Deseure, M. Chatenet, J. Carrey, B. Chaudret, A. Rouet, *Nature Energy* **2018**, *3*, 476.

[27] B. Chang, S. Hao, Z. Ye, Y. Yang, *Chemical Communications* **2018**, *54*, 2393.

[28] H. Xia, Z. Huang, C. Lv, C. Zhang, *ACS Catalysis* **2017**, *7*, 8205.

[29] E. Zolotoyabko, *Advanced Materials Interfaces* **2017**, *4*, 1600189.

[30] Q. Shi, S. Fu, C. Zhu, J. Song, D. Du, Y. Lin, *Materials Horizons* **2019**, *6*, 684.

[31] G. F. Chen, T. Y. Ma, Z. Q. Liu, N. Li, Y. Z. Su, K. Davey, S. Z. Qiao, *Advanced Functional Materials* **2016**, *26*, 3314.

[32] B. You, N. Jiang, M. Sheng, M. W. Bhushan, Y. Sun, *Acs Catalysis* **2016**, *6*, 714.

[33] H. Wang, D. Yong, S. Chen, S. Jiang, X. Zhang, W. Shao, Q. Zhang, W. Yan, B. Pan, Y. Xie, *Journal of the American Chemical Society* **2018**, *140*, 1760.

[34] X. Yang, Y. Tian, S. Mukherjee, K. Li, X. Chen, J. Lv, S. Liang, L.-K. Yan, G. Wu, H.-Y. Zang, *Angewandte Chemie International Edition* **2023**, *62*, e202304797.

[35] A. Grimaud, O. Diaz-Morales, B. Han, W. T. Hong, Y.-L. Lee, L. Giordano, K. A. Stoerzinger, M. T. Koper, Y. Shao-Horn, *Nature chemistry* **2017**, *9*, 457.

[36] P. Zhang, L. Li, D. Nordlund, H. Chen, L. Fan, B. Zhang, X. Sheng, Q. Daniel, L. Sun, *Nature communications* **2018**, *9*, 1.

[37] S. M. Kim, P. M. Abdala, T. Margossian, D. Hosseini, L. Foppa, A. Armutlulu, W. van Beek, A. Comas-Vives, C. Copéret, C. Müller, *Journal of the American Chemical Society* **2017**, *139*, 1937.

[38] O. Margeat, D. Ciuculescu, P. Lecante, M. Respaud, C. Amiens, B. Chaudret, *Small* **2007**, *3*, 451.

[39] X. Long, J. Li, S. Xiao, K. Yan, Z. Wang, H. Chen, S. Yang, *Angewandte Chemie* **2014**, *126*, 7714.

[40] L. Trotochaud, S. L. Young, J. K. Ranney, S. W. Boettcher, *Journal of the American Chemical Society* **2014**, *136*, 6744.

[41] B. S. Yeo, A. T. Bell, *The Journal of Physical Chemistry C* **2012**, *116*, 8394.

[42] B. C. Cornilsen, X. Shan, P. L. Loyselle, *Journal of power sources* **1990**, *29*, 453.

[43] H. Osgood, S. V. Devaguptapu, H. Xu, J. Cho, G. Wu, *Nano Today* **2016**, *11*, 601.

[44] L. Guo, S. Hwang, B. Li, F. Yang, M. Wang, M. Chen, X. Yang, S. G. Karakalos, D. A. Cullen, Z. Feng, G. Wang, G. Wu, H. Xu, *ACS Nano* **2021**, *15*, 6886.

[45] X. Ren, T. Wu, Y. Sun, Y. Li, G. Xian, X. Liu, C. Shen, J. Gracia, H.-J. Gao, H. Yang, Z. J. Xu, *Nature Communications* **2021**, *12*, 2608.

[46] C. Wei, Z. J. Xu, *Chinese Journal of Catalysis* **2022**, *43*, 148.

[47] F. A. Garcés-Pineda, M. Blasco-Ahicart, D. Nieto-Castro, N. López, J. R. Galán-Mascarós, *Nature Energy* **2019**, *4*, 519.

[48] X. Ren, T. Wu, Z. Gong, L. Pan, J. Meng, H. Yang, F. B. Dagbjartsdottir, A. Fisher, H.-J. Gao, Z. J. Xu, *Nature Communications* **2023**, *14*, 2482.

[49] S. Luo, K. Elouarzaki, Z. J. Xu, *Angewandte Chemie International Edition* **2022**, *61*, e202203564.

[50] X. Ren, T. Wu, Y. Sun, Y. Li, G. Xian, X. Liu, C. Shen, J. Gracia, H.-J. Gao, H. Yang, *Nature communications* **2021**, *12*, 1.

[51] X. Li, Z. Cheng, X. Wang, *Electrochemical Energy Reviews* **2021**, *4*, 136.

[52] F. Dionigi, Z. Zeng, I. Sinev, T. Merzdorf, S. Deshpande, M. B. Lopez, S. Kunze, I. Zegkinoglou, H. Sarodnik, D. Fan, A. Bergmann, J. Drnec, J. F. d. Araujo, M. Gliech, D. Teschner, J. Zhu, W.-X. Li, J. Greeley, B. R. Cuenya, P. Strasser, *Nature Communications* **2020**, *11*, 2522.

[53] F. Dionigi, J. Zhu, Z. Zeng, T. Merzdorf, H. Sarodnik, M. Gliech, L. Pan, W.-X. Li, J. Greeley, P. Strasser, *Angewandte Chemie International Edition* **2021**, *60*, 14446.

[54] Z. Lu, L. Qian, Y. Tian, Y. Li, X. Sun, X. Duan, *Chemical Communications* **2016**, *52*, 908.

[55] B. Ravel, M. Newville, *Journal of Synchrotron Radiation* **2005**, *12*, 537.

**The table of contents entry**

In this work, we developed a new class of ternary NiFeM (M: Cu, Co, and Mn) metallic glassy nanofoam network catalysts with adequate surface areas/porosity and electrical conductivity, which was thoroughly studied in the alkaline anion-exchange membrane water electrolyzers (AEMWEs). This is the first demonstration that PGM-free anode catalysts can perform better than state-of-the-art precious metal catalysts in real AEMWEs.

*Xiaoxuan Yang,[Δ] Jiashun Liang,[Δ] Qiurong Shi,[Δ] Michael Zachman,[Δ] Sadia Kabir, Junwu Liang, Jing Zhu, Benjamin Slenker, Max Pupucevski, Natalia Macauley, A. Jeremy Kropf, Hao Zeng, Derek Strasser, Deborah J. Myers,* Hui Xu,* Zhenhua Zeng,* Yushan Yan, and Gang Wu**

# Regulating the Third Metal to Design and Engineer Multilayered NiFeM (M: Co, Mn, and Cu) Nanofoam Anode Catalysts for Anion-Exchange Membrane Water Electrolyzers

ToC figure